Nodeless superconductivity in the centro- and noncentrosymmetric rhenium-boron superconductors

T. Shang,[1,*] W. Xie,[2,†] J. Z. Zhao,[3,4] Y. Chen,[2] D. J. Gawryluk,[5]
M. Medarde,[5] M. Shi,[6] H. Q. Yuan,[2] E. Pomjakushina,[5] and T. Shiroka[7,8]

[1]*Key Laboratory of Polar Materials and Devices (MOE), School of Physics and Electronic Science, East China Normal University, Shanghai 200241, China*
[2]*Center for Correlated Matter and Department of Physics, Zhejiang University, Hangzhou 310058, China*
[3]*Co-Innovation Center for New Energetic Materials, Southwest University of Science and Technology, Mianyang, 621010, China*
[4]*Research Laboratory for Quantum Materials, Singapore University of Technology and Design, Singapore 487372, Singapore*
[5]*Laboratory for Multiscale Materials Experiments, Paul Scherrer Institut, Villigen CH-5232, Switzerland*
[6]*Swiss Light Source, Paul Scherrer Institut, Villigen CH-5232, Switzerland*
[7]*Laboratory for Muon-Spin Spectroscopy, Paul Scherrer Institut, Villigen PSI, Switzerland*
[8]*Laboratorium für Festkörperphysik, ETH Zürich, CH-8093 Zürich, Switzerland*

We report a comprehensive study of the centrosymmetric Re_3B and noncentrosymmetric Re_7B_3 superconductors. At a macroscopic level, their bulk superconductivity (SC), with $T_c = 5.1$ K (Re_3B) and 3.3 K (Re_7B_3), was characterized via electrical-resistivity, magnetization, and heat-capacity measurements, while their microscopic superconducting properties were investigated by means of muon-spin rotation/relaxation (μSR). In both Re_3B and Re_7B_3 the low-T zero-field electronic specific heat and the superfluid density (determined via tranverse-field μSR) suggest a nodeless SC. Both compounds exhibit some features of multigap SC, as evidenced by temperature-dependent upper critical fields $H_{c2}(T)$, as well as by electronic band-structure calculations. The absence of spontaneous magnetic fields below the onset of SC, as determined from zero-field μSR measurements, indicates a preserved time-reversal symmetry in the superconducting state of both Re_3B and Re_7B_3. Our results suggest that a lack of inversion symmetry and the accompanying antisymmetric spin-orbit coupling effects are not essential for the occurrence of multigap SC in these rhenium-boron compounds.

I. INTRODUCTION

The possibility to host unconventional- and topological superconductivity (SC), or to act as systems where to realize the Majorana fermions [1–11], has made noncentrosymmetric superconductors (NCSCs) one the most investigated families in recent times. In NCSCs, a lack of inversion symmetry implies that admixtures of spin-singlet and spin-triplet superconducting pairings are allowed [1–3]. This sets the scene for a variety of exotic properties, such as, upper critical fields beyond the Pauli limit [12, 13], nodes in the superconducting gap [14–17], or multigap SC [18]. More interestingly, by using the muon-spin relaxation (μSR) technique, time-reversal symmetry (TRS) breaking has been observed to occur in the superconducting state of selected weakly-correlated NCSCs. These include CaPtAs [17], $LaNiC_2$ [19], La_7T_3 (T = transition metal) [20–22], Zr_3Ir [23], and ReT [24–27]. Except for CaPtAs, where TRS breaking and superconducting gap nodes coexist below T_c [17, 28], in most other cases the superconducting properties resemble those of conventional superconductors, characterized by a fully opened energy gap. In general, the causes behind TRS breaking in these superconductors are not yet fully understood and remain an intriguing open question.

To clarify the issue, the α-Mn-type ReT superconductors have been widely studied and demonstrated to show a superconducting state with broken TRS [24–27]. Our previous comparative μSR studies on Re-Mo alloys, covering four different crystal structures (including the noncentrosymmetric α-Mn-type), reveal that the spontaneous magnetic fields occurring below T_c were only observed in elementary rhenium and in $Re_{0.88}Mo_{0.12}$ [27, 29, 30]. By contrast, TRS was preserved in the Re-Mo alloys with a lower Re-content (below $\sim$ 88%), independent of their centro- or noncentrosymmetric crystal structures [30]. Since both elementary rhenium and $Re_{0.88}Mo_{0.12}$ adopt a simple centrosymmetric structure (hcp-Mg-type), this strongly suggests that a noncentrosymmetric structure is not essential in realizing the TRS breaking in ReT superconductors. The μSR results regarding the Re-Mo family, as well as other α-Mn-type superconductors, e.g., $Mg_{10}Ir_{19}B_{16}$, $Nb_{0.5}Os_{0.5}$, Re_3W, and Re_3Ta [31–34], where TRS is preserved, clearly indicate that not only the Re presence, but also its amount is crucial for the appearance and the extent of TRS breaking in the ReT superconductors. How these results can be understood within a more general framework clearly requires further investigations.

Rhenium-boron compounds represent another suitable candidate system for studying the TRS breaking effects in the family of Re-based superconductors. Indeed, upon slight changes of the Re/B ratio, both centrosymmetric Re_3B (C-Re_3B) and noncentrosymmetric Re_7B_3 (NC-Re_7B_3) compounds can be synthesized [35], the latter adopting the same Th_7Fe_3-type structure as La_7T_3 superconductors [20–22], which frequently exhibit broken TRS in the superconducting state. Although selected properties of Re_3B and Re_7B_3 have been investigated by different techniques [36–38], their superconducting properties at a microscopic level, in particular, the superconducting order parameter, require further investigations.

In this paper, we report on a comprehensive study of the superconducting properties of Re_3B and Re_7B_3, carried out via electrical-resistivity, magnetization, heat-capacity, and muon-spin relaxation/rotation (μSR) measurements, as well as by electronic band-structure calculations. Our endeavors served a dual purpose. Firstly, since La_7T_3 shows evidence of TRS breaking below T_c, it is of interest to establish if also the isostructural Re_7B_3 compound shows similar features. Secondly, by systematically investigating the C-Re_3B and

* Corresponding authors:
tshang@phy.ecnu.edu.cn
† Present address: Deutsches Elektronen-Synchrotron (DESY), Notkestraße 85, 22607 Hamburg, Germany

NC-Re_7B_3 superconductors, the previous findings regarding the ReT family can be extended also to other NCSC families, thus providing further insight into the open question of TRS breaking in NCSCs.

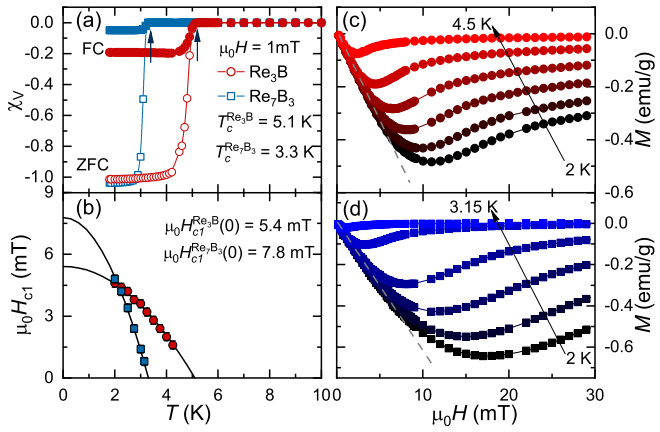

FIG. 1. (a) Temperature-dependent magnetic susceptibility of Re_3B and Re_7B_3, measured in an applied field of 1 mT using the ZFC and FC protocols. (b) Lower critical fields H_{c1} vs. temperature. Solid lines are fits to $\mu_0 H_{c1}(T) = \mu_0 H_{c1}(0)[1-(T/T_c)^2]$. Field-dependent magnetization recorded at various temperatures for Re_3B (c) and Re_7B_3 (d). For each temperature, H_{c1} was determined as the value where $M(H)$ starts deviating from linearity (see dashed lines).

II. EXPERIMENTAL AND NUMERICAL METHODS

Polycrystalline rhenium-boron compounds were prepared by arc melting Re (99.99%, ChemPUR) and B (99.995%, ChemPUR) powders with different stoichiometric ratios in a high-purity argon atmosphere. To improve the homogeneity, samples were flipped and remelted several times and, finally, annealed at 800°C for two weeks. The x-ray powder diffraction, measured using a Bruker D8 diffractometer with Cu Kα radiation, confirmed the orthorhombic centrosymmetric structure of Re_3B ($Cmcm$, No. 63), and the hexagonal noncentrosymmetric structure of Re_7B_3 ($P6_3mc$, No. 186) (see details in Fig. S1) [39]. The magnetization, electrical-resistivity, and heat-capacity measurements were performed on Quantum Design MPMS and PPMS instruments, respectively. The bulk μSR measurements were carried out at the multipurpose surface-muon spectrometer (Dolly) of the Swiss muon source at Paul Scherrer Institut, Villigen, Switzerland. The μSR data were analyzed by means of the `musrfit` software package [40].

The electronic band structures of Re_3B and Re_7B_3 were calculated via the density functional theory (DFT), within the generalized gradient approximation (GGA) of Perdew-Burke-Ernzerhof (PBE) realization [41], as implemented in the QUANTUM ESPRESSO [42, 43]. The projector augmented wave (PAW) pseudopotentials were adopted for the calculation [44, 45]. Electrons belonging to the outer atomic configuration were treated as valence electrons, here corresponding to 15 electrons in Re ($5s^2 5p^6 5d^5 6s^2$), and 3 electrons in B ($2s^2 2p^1$). The kinetic energy cutoff was fixed to 55 Ry. For the self-consistent calculation, the Brillouin zone integration was performed on a Γ-centered mesh of $15 \times 15 \times 10$ k-points for Re_3B and $12 \times 12 \times 18$ k-points for Re_7B_3. Experimentally determined lattice constants and atom positions were used in this calculation.

III. RESULTS AND DISCUSSION

The bulk superconductivity of C-Re_3B and NC-Re_7B_3 was first characterized by magnetic susceptibility measurements, using both field-cooled (FC) and zero-field-cooled (ZFC) protocols in an applied field of 1 mT. As indicated by the arrows in Fig. 1(a), a clear diamagnetic signal appears below the superconducting transition at $T_c = 5.1$ K and 3.3 K for Re_3B and Re_7B_3, respectively. After accounting for the demagnetization factor, the superconducting shielding fraction of both samples is close to 100%, indicative of bulk SC, which was further confirmed by heat-capacity measurements [39]. To determine the lower critical field H_{c1}, essential for performing μSR measurements on type-II superconductors, the field-dependent magnetization $M(H)$ was collected at various temperatures. Some representative $M(H)$ curves are shown in Figs. 1(c) and (d) for Re_3B and Re_7B_3, respectively. The estimated H_{c1} values as a function of temperature are summarized in Fig. 1(b), resulting in $\mu_0 H_{c1}(0) = 5.4(1)$ mT and 7.8(1) mT for Re_3B and Re_7B_3, respectively.

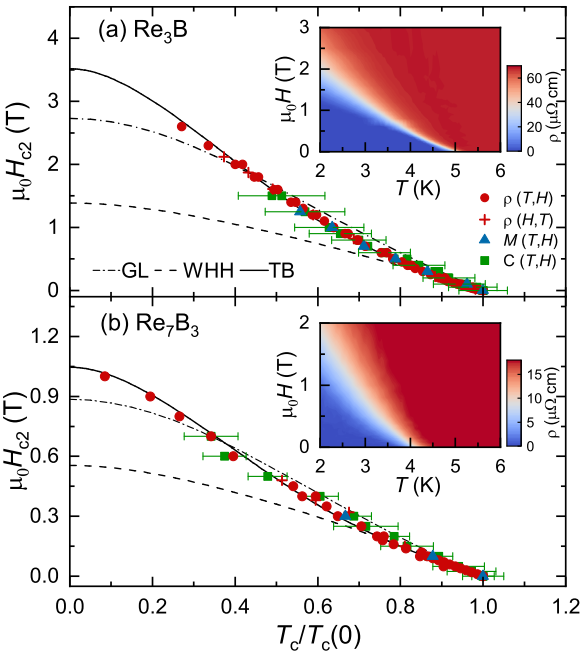

FIG. 2. Upper critical fields H_{c2} vs. reduced temperature $T_c/T_c(0)$ for Re_3B (a) and Re_7B_3 (b), as determined from temperature-dependent electrical resistivity $\rho(T,H)$, magnetization $M(T,H)$, and heat capacity $C(T,H)$, and from field-dependent electrical resistivity $\rho(H,T)$. The contour plots of $\rho(T,H)$ in the insets indicate a clear positive curvature close to T_c. Three different models, including the GL- (dash-dotted line), WHH- (dashed line), and TB models (solid line), were used to analyze the $H_{c2}(T)$ data. Note the positive curvature visible near $\mu_0 H \sim 1$ T and 0.2 T for Re_3B and Re_7B_3, respectively. The error bars refer to the superconducting transition widths ΔT_c in the specific-heat data.

The upper critical field H_{c2} of Re_3B and Re_7B_3 was determined from measurements of the electrical resistivity, magnetization, and heat capacity under various magnetic fields up to 3 T (see Fig. S2 for details) [39]. In zero magnetic field, the T_c values determined from different methods are highly consistent. The upper critical fields are summarized in Figs. 2(a) and (b) versus the reduced superconducting transition temperature $T_c/T_c(0)$ for Re_3B and Re_7B_3, respectively. The $H_{c2}(T)$ was analyzed by means of Ginzburg–Landau

(GL) [46], Werthamer–Helfand–Hohenberg (WHH) [47], and two-band (TB) models [48]. As shown in Fig. 2, both GL- and WHH models can reasonably describe the $H_{c2}(T)$ at low fields, i.e., $\mu_0 H_{c2} < 0.5$ T (0.2 T) for Re_3B (Re_7B_3). While at higher magnetic fields, both models deviate significantly from the experimental data and provide underestimated H_{c2} values. Such discrepancy most likely hints at multiple superconducting gaps in Re_3B and Re_7B_3, as evidenced also by the positive curvature of $H_{c2}(T)$, a typical feature of multigap superconductors, as e.g., $Lu_2Fe_3Si_5$ [49], MgB_2 [50, 51], or the recently reported Mo_5PB_2 [52]. Physically, the positive curvature reflects the gradual suppression of the small superconducting gap upon increasing the magnetic field. As clearly demonstrated in the insets of Fig. 2, the $H_{c2}(T)$ of Re_3B and Re_7B_3 exhibit clear kinks close to 0.5 and 0.2 T, respectively, most likely coinciding with the field values able to suppress the smaller gap. As shown by the solid lines in Fig. 2, the TB model shows a remarkable agreement with the experimental data and provides $\mu_0 H_{c2}(0) = 3.5(1)$ T and 1.05(5) T for Re_3B and Re_7B_3, respectively.

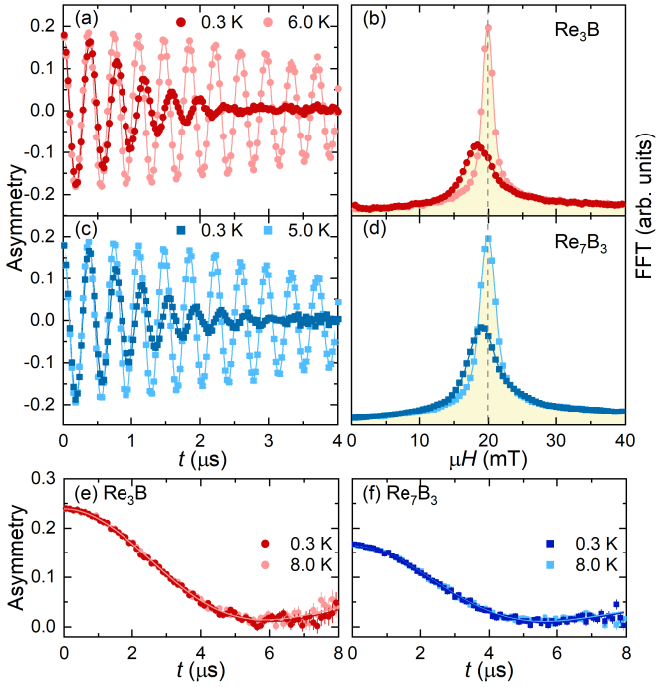

FIG. 3. (a) TF-μSR spectra of Re_3B collected in the superconducting- (0.3 K) and the normal state (6 K) in an applied magnetic field of 20 mT. (b) Fast Fourier transforms of the TF-μSR data shown in (a). Panels (c) and (d): the analogous results for the Re_7B_3 case. The solid lines through the data are fits to Eq. (1), while the vertical dashed line marks the applied magnetic field. Note the clear diamagnetic shift and the field broadening at 0.3 K, as shown in (b) and (d). ZF-μSR spectra of Re_3B (e) and Re_7B_3 (f), collected in the superconducting and the normal states. Solid lines are fits using the equation described in the text. The overlapping datasets indicate no evident changes with temperature.

To investigate at a microscopic level the SC of Re_3B and Re_7B_3, we carried out systematic transverse-field (TF) μSR measurements in an applied field of 20 mT, i.e., more than twice their $\mu_0 H_{c1}(0)$ values [see Fig. 1(b)]. Representative TF-μSR spectra collected in the superconducting- and normal states of Re_3B and Re_7B_3 are shown in Figs. 3(a) and (c), respectively. The additional field distribution broadening due to flux-line lattice (FLL) in the mixed state is clearly visible in Figs. 3(b) and (d), where the fast-Fourier-transform (FFT) spectra of the corresponding TF-μSR data are presented. To describe the asymmetric field distribution (e.g., see FFT at 0.3 K), the TF-μSR spectra were modeled using:

$$A(t) = \sum_{i=1}^{n} A_i \cos(\gamma_\mu B_i t + \phi) e^{-\sigma_i^2 t^2/2} + A_{bg} \cos(\gamma_\mu B_{bg} t + \phi). \quad (1)$$

Here A_i, A_{bg} and B_i, B_{bg} are the asymmetries and local fields sensed by implanted muons in the sample and sample holder (copper, which normally shows zero muon-spin depolarization), $\gamma_\mu/2\pi = 135.53$ MHz/T is the muon gyromagnetic ratio, ϕ is a shared initial phase, and σ_i is the Gaussian relaxation rate of the ith component. As shown by solid lines in Fig. 3(a) to (d), two oscillations (i.e., $n = 2$) are required to properly describe the TF-μSR spectra for both Re_3B and Re_7B_3. The derived $\sigma_i(T)$ as a function of temperature are summarized in the insets of Fig. 4. Above T_c, $\sigma_i(T)$ values are small and temperature-independent, but below T_c they start to increase due to the onset of FLL and the increased superfluid density. Simultaneously, a diamagnetic field shift appears below T_c, given by $\Delta B(T) = \langle B \rangle - B_{appl.}$, with $\langle B \rangle = (A_1 B_1 + A_2 B_2)/A_{tot}$, $A_{tot} = A_1 + A_2$, and $B_{appl.}$ the applied field. The effective Gaussian relaxation rate can be estimated from $\sigma_{eff}^2/\gamma_\mu^2 = \sum_{i=1}^{2} A_i[\sigma_i^2/\gamma_\mu^2 + (B_i - \langle B \rangle)^2]/A_{tot}$ [53]. Considering the constant nuclear relaxation rate σ_n in the narrow temperature range investigated here, confirmed also by zero-field (ZF) μSR measurements [see details in Figs. 3(e) and (f) and Table S1] [39], the superconducting contribution can be extracted using $\sigma_{sc} = \sqrt{\sigma_{eff}^2 - \sigma_n^2}$. Then, the effective magnetic penetrate depth λ_{eff} and thus, the superfluid density ρ_{sc} ($\propto \lambda_{eff}^{-2}$) can be calculated following $\sigma_{sc} = 0.172 \frac{\gamma_\mu \Phi_0}{2\pi}(1-h)[1 + 1.21(1-\sqrt{h})^3]\lambda_{eff}^{-2}$ [54, 55], where $h = H_{appl}/H_{c2}$, with $\mu_0 H_{appl} = 20$ mT the applied magnetic field.

We also performed ZF-μSR measurements in both the normal- and the superconducting states of Re_3B and Re_7B_3. As shown in Figs. 3(e) and (f), neither coherent oscillations nor fast decays could be identified in the spectra collected above (8 K) and below T_c (0.3 K), hence implying the lack of any magnetic order or fluctuations. The weak muon-spin relaxation in absence of an external magnetic field is mainly due to the randomly oriented nuclear moments, which can be modeled by means of a phenomenological relaxation function, consisting of a combination of Gaussian- and Lorentzian Kubo-Toyabe relaxations [56, 57], $A(t) = A_s[\frac{1}{3} + \frac{2}{3}(1 - \sigma_{ZF}^2 t^2 - \Lambda_{ZF} t)e^{(-\frac{\sigma_{ZF}^2 t^2}{2} - \Lambda_{ZF} t)}] + A_{bg}$. Here A_s ($\equiv A_{tot}$) and A_{bg} are the same as in the TF-μSR case [see Eq. 1]. The σ_{ZF} and Λ_{ZF} represent the zero-field Gaussian and Lorentzian relaxation rates, respectively. As shown by the solid lines in Figs. 3(e) and (f), the derived relaxations in the normal- and the superconducting states are almost identical (see Table S1) [39], as confirmed also by the practically overlapping ZF-μSR spectra above and below T_c. This lack of evidence for an additional μSR relaxation below T_c excludes a possible TRS breaking in the superconducting state of both C-Re_3B and NC-Re_7B_3.

The superfluid density ρ_{sc} vs. the reduced T/T_c are shown in Figs. 4(a) and (b) for Re_3B and Re_7B_3, respectively. The temperature-independent superfluid density below $T_c/3$ indicates a fully-gapped SC in both cases. Therefore, we analyzed the $\rho_{sc}(T)$ by means of a fully-gapped s-wave model:

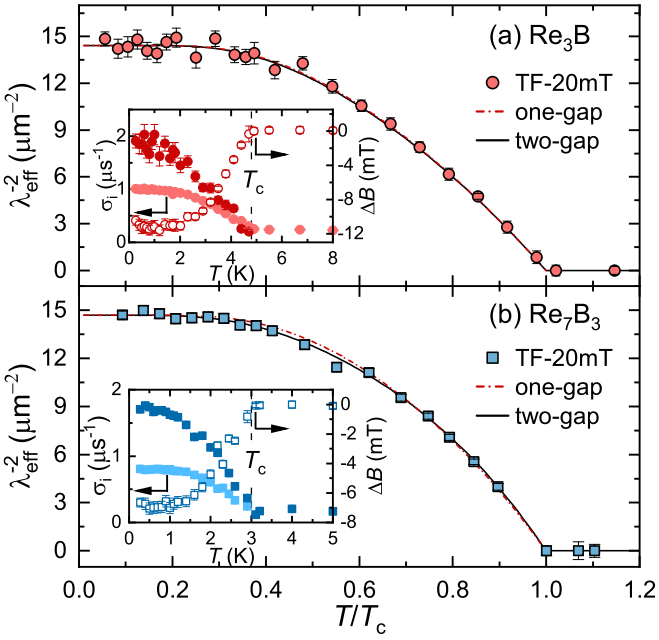

FIG. 4. Superfluid density vs. reduced temperature T/T_c for Re_3B (a) and Re_7B_3 (b). The insets show the temperature-dependent muon-spin relaxation rate $\sigma_i(T)$ (left-axis) and the diamagnetic shift $\Delta B(T)$ (right-axis). The dashed lines in the insets indicate the T_c values, while the dash-dotted- and solid lines in the main panels represent fits to a fully-gapped s-wave model with one- and two gaps, respectively.

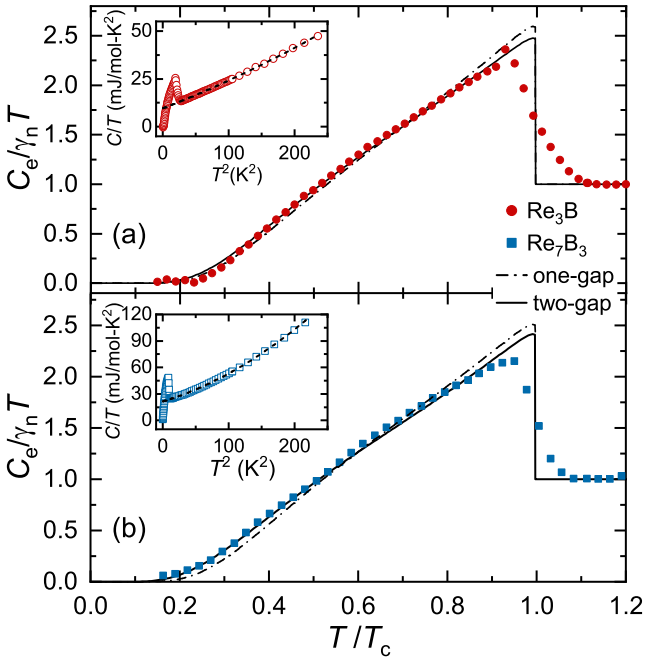

FIG. 5. Normalized electronic specific heat $C_e/\gamma_n T$ versus reduced temperature T/T_c for Re_3B (a) and Re_7B_3 (b). γ_n is the normal-state electronic specific-heat coefficient. The insets show the measured specific heat C/T versus T^2. The dashed-lines in the insets are fits to $C/T = \gamma_n + \beta T^2 + \delta T^4$ for $T > T_c$, while the dash-dotted- and solid lines in the main panel represent the electronic specific heat calculated by considering a fully-gapped s-wave model with one- and two gaps, respectively.

$$\rho_{sc}(T) = \frac{\lambda_{eff}^{-2}(T)}{\lambda_0^{-2}} = 1 + 2\int_{\Delta(T)}^{\infty} \frac{\partial f}{\partial E} \frac{EdE}{\sqrt{E^2 - \Delta^2(T)}}. \quad (2)$$

Here $f = (1 + e^{E/k_BT})^{-1}$ and $\Delta(T)$ are the Fermi- and the superconducting-gap functions. The $\Delta(T)$ is assumed to follow $\Delta(T) = \Delta_0 \tanh\{1.82[1.018(T_c/T - 1)]^{0.51}\}$ [58], where Δ_0 is the superconducting gap at 0 K. Since the upper critical field H_{c2}(T) exhibits typical features of multigap SC (see Fig. 2), the superfluid density was fitted using Eq. (2) with one- and two gaps. In the two-gap case, $\rho_{sc}(T) = w\rho_{sc}^{\Delta^f}(T) + (1-w)\rho_{sc}^{\Delta^s}(T)$, with $\rho_{sc}^{\Delta^f}$ and $\rho_{sc}^{\Delta^s}$ being the superfluid densities related to the first- (Δ^f) and second (Δ^s) gap, and w a relative weight. For Re_3B, both the one- and two-gap models show an almost identical goodness-of-fit parameter ($\chi_r^2 \sim 1.2$), reflected in two practically overlapping fitting curves in Fig. 4(a). For Re_7B_3, instead, the two-gap model ($\chi_r^2 \sim 1.1$) is slightly superior to the one-gap model ($\chi_r^2 \sim 2.2$) [see Fig. 4(b)]. For the two-gap model, in the Re_3B case, the derived zero-temperature magnetic penetration depth is $\lambda_0 = 263(2)$ nm, the gap values are $\Delta_0^f = 0.72(1)$ meV and $\Delta_0^s = 0.87(2)$ meV, with a weight $w = 0.7$. In the Re_7B_3 case, the corresponding values are λ_0 =261(2) nm, $\Delta_0^f = 0.35(1)$ meV and $\Delta_0^s = 0.57(2)$ meV, with $w = 0.27$. For the one-gap model, the gap values are $\Delta_0 = 0.77(2)$ and 0.50(2) meV for Re_3B and Re_7B_3, with the same λ_0 values as in the two-gap case.

Unlike in the clean-limit case ($\xi_0 \ll l_e$) [see Eq. (2)], in the dirty limit, the BCS coherence length ξ_0 is much larger than the electronic mean-free path l_e. In the BCS approximation, the temperature dependent superfluid density in the dirty limit is given by [59]:

$$\rho_{sc}(T) = \frac{\Delta(T)}{\Delta_0} \tanh\left[\frac{\Delta(T)}{2k_BT}\right], \quad (3)$$

where $\Delta(T)$ is the same as in Eq. (2). For Re_3B, ξ_0 is larger than l_e ($\xi_0/l_e \sim 7.7$), therefore, Re_3B is close to the dirty limit; while for Re_7B_3, ξ_0 is smaller than l_e ($\xi_0/l_e \sim 0.3$), i.e., it is close to the clean limit. For both compounds, the ξ_0 and l_e are not significantly different and exhibit similar magnitudes. Hence, both Eq. (2) and Eq. (3) describe quite well the low-T superfluid density, and yield similar superconducting gaps (see Table I).

To further support the indications of a multigap SC obtained from H_{c2}, we measured also the zero-field specific heat down to $1/3T_c$. After subtracting the phonon contribution ($\beta T^2 + \delta T^4$) from the measured data, the obtained electronic specific heat divided by the γ_n, i.e., $C_e/\gamma_n T$, is shown in Fig. 5(a) and (b) vs. the reduced temperature T/T_c for Re_3B and Re_7B_3, respectively. The superconducting-phase contribution to the entropy can be calculated following the BCS expression [59]:

$$S(T) = -\frac{6\gamma_n}{\pi^2 k_B}\int_0^{\infty} [f\ln f + (1-f)\ln(1-f)]\,d\epsilon, \quad (4)$$

where f is the same as in Eq. (2). Then, the temperature-dependent electronic specific heat below T_c can be obtained from $C_e(T) = T\frac{dS(T)}{dT}$. The dash-dotted lines in Fig. 5 represent fits of an s-wave model with $\gamma_n = 9.6(1)$ and 21.5(2) mJ/mol-K^2 and a single gap $\Delta_0 = 0.75(2)$ and 0.47(1) meV for Re_3B and Re_7B_3, respectively. For Re_7B_3, while the one-gap model reproduces the data for

$T/T_c \gtrsim 0.5$, it deviates from them at lower temperatures, hence yielding a slightly larger $\chi_r^2 \sim 7.8$ than the two-gap model (see below). On the contrary, the two-gap model exhibits a better agreement with the experimental data. The solid line in Fig. 5(b) is a fit with two energy gaps, i.e., $C_e(T)/T = wC_e^{\Delta^f}(T)/T + (1-w)C_e^{\Delta^s}(T)/T$. Here, each term represents a one-gap specific-heat contribution, with w, Δ^f, and Δ^s being the same parameters as in case of superfluid density fits. In Re_7B_3, by sharing the w values, the two-gap model gives $\Delta_0^f = 0.32(1)$ meV and $\Delta_0^s = 0.50(1)$ meV, with $\chi_r^2 \sim 1.7$. Similarly, in Re_3B, the solid-line in Fig. 5(a) is a fit with $\Delta_0^f = 0.69(2)$ meV and $\Delta_0^s = 0.79(2)$ meV. For Re_3B, although the two-gap model agrees slightly better with the experimental data for $T/T_c > 0.4$, below it, both one-gap and two-gap models deviate slightly from the measured data, probably reflecting an improper subtraction of the nuclear Schottky contribution (due to the limited lowest temperature that could be reached in this study — see details in Fig. S3) [39]. Measurements of zero-field specific heat down to the mK range are highly demanded to confirm the multigap nature of Re_3B and Re_7B_3. Note that, for both compounds, the superconducting parameters determined from the specific heat and the TF-μSR are highly consistent (see Table I).

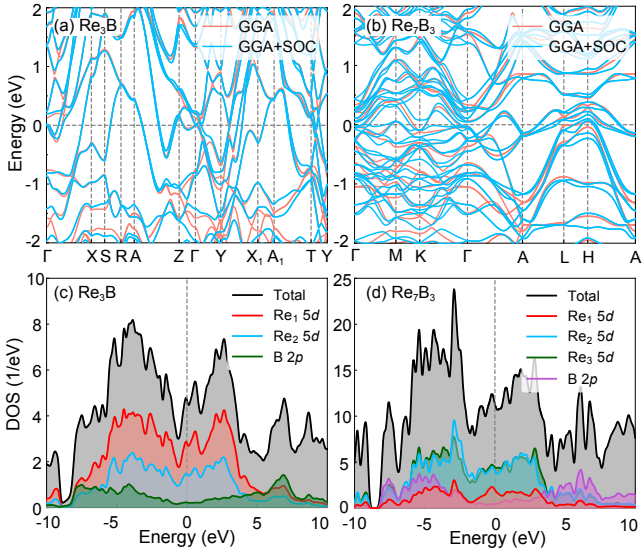

FIG. 6. Electronic band structure of C-Re_3B (a) and NC-Re_7B_3 (b), calculated by ignoring (red) and by considering (blue) the spin-orbit coupling. For both compounds, various bands which cross the Fermi level can be identified. The total and partial (Re 5d and B 2p orbitals) density of states are shown in panels (c) and (d) for Re_3B and Re_7B_3, respectively.

Further evidence on the multigap SC and insight into the electronic properties of Re_3B and Re_7B_3 comes from band-structure calculations. The electronic band structures, as well as the density of states (DOS) are shown in Fig. 6. As can be seen from Figs. 6(a) and (b), 4 and 12 different bands cross the Fermi level in Re_3B and Re_7B_3, respectively. Close to E_F, the DOS of both compounds is dominated by the Re 5d orbitals, while the contribution from the B 2p orbitals is negligible [see Figs. 6(a) and (b) and Fig. S4 [39]]. Away from the Fermi level, the Re 5d and B 2p orbitals are highly hybridized. The estimated DOS at E_F are ~ 4.7 and ~ 11.4 states/(eV·u.c.) for Re_3B and Re_7B_3, both comparable to the experimental values determined from electronic specific heat coefficient (see Table I). We expect the multigap features of Re_3B and Re_7Be_3, to be closely related to the different site symmetries of Re atoms in the unit cell. For Re_3B, according to band-structure calculations, the contribution of Re1 (8f) atoms to the DOS is comparable to that of Re2 (4c) atoms [see Figs. 6(c)]. While for Re_7B_3, the contribution of Re2 (6c) and Re3 (6c) atoms is preponderant compared to that of Re1 (2b) atoms.

Now, let us compare the superconducting parameters of Re_3B and Re_7B_3 with those of other superconductors. First, by using the SC parameters obtained from the measurements presented here, we calculated an effective Fermi temperature $T_F = 1.0(1)\times10^4$ and $0.25(1)\times10^4$ K for Re_3B and Re_7B_3 (see other parameters in Table I). T_F is proportional to $n_s^{2/3}/m^\star$, where n_s and $m^\star$ are the carrier density and the effective mass. Consequently, the different families of superconductors can be classified according to their T_c/T_F ratios into a so-called Uemura plot [60]. Several types of unconventional superconductors, including heavy fermions, organics, high-T_c iron pnictides, and cuprates, all lie in a $10^{-2} < T_c/T_F < 10^{-1}$ band (gray region in Fig. S5) [39]. Conversely, many conventional superconductors, e.g., Al, Sn, and Zn, are located at $T_c/T_F < \sim 10^{-4}$. Between these two categories lie several multigap superconductors, e.g., $LaNiC_2$, Nb_5Ir_3O, $ReBe_{22}$, $NbSe_2$, and MgB_2 [60–64]. Although there is no conclusive evidence for them to be classified as unconventional superconductors, the rhenium-boron superconductors lie clearly far off the conventional band. For Re_3B, $T_c/T_F = 4.8\times10^{-4}$ is almost identical to the analogous value for multigap $ReBe_{22}$ and $LaNiC_2$, the latter representing a typical example of NCSCs. While for Re_7B_3, the $T_c/T_F = 1.16\times10^{-3}$ is very close to the multigap Nb_5Ir_3O and elementary rhenium superconductors [27, 30, 63], the latter showing a breaking of TRS in the superconducting state and exhibiting a centrosymmetric crystal structure. In general, most of the weakly-correlated NCSCs, e.g., ReT, Mo_3Al_2C, $Li_2(Pd, Pt)_3B$, and $LaNiC_2$, exhibit a T_c/T_F between the unconventional and conventional bands [64], which is also the case for Re_7B_3.

Second, we discuss why the multigap feature is more evident in Re_7B_3 than in Re_3B, both in the temperature-dependent superfluid density and the zero-field electronic specific data. In general, if the weight of the second gap is relatively small and the gap sizes are not significantly different, this makes it difficult to discriminate between a single- and a two-gap superconductor based on temperature-dependent superconducting properties. For Re_3B, the weight of the second gap $w = 0.3$ is similar to that of Re_7B_3 ($w = 0.27$). However, the gap sizes are clearly distinct in Re_7B_3 ($\Delta^f/\Delta^s \sim 0.6$) compared to Re_3B ($\Delta^f/\Delta^s \sim 0.9$). As a consequence, the multigap feature is more evident in Re_7B_3. On the other hand, from the analysis of $H_{c2}(T)$ using a two-band model, the derived inter-band and intra-band couplings are $\lambda_{12} = 0.08$ and $\lambda_{11} \sim \lambda_{22} = 0.4$, and $\lambda_{12} = 0.01$ and $\lambda_{11} \sim \lambda_{22} = 0.15$ for Re_3B and Re_7B_3, respectively. In both cases, the inter-band coupling is much smaller than the intra-band coupling. In addition, the inter-band coupling of Re_3B (0.08) is larger than that of Re_7B_3 (0.01). This makes the gaps to open at different electronic bands, less distinguishable in the former case [65]. Despite these differences, the underlying multigap SC feature of both samples is reflected in their upper critical fields $H_{c2}(T)$ (see Fig. 2). To get further insight into the multigap SC of Re_3B and Re_7B_3, the measurement of the *field*-dependent superconducting Gaussian relaxation

rate $\sigma_{sc}(H)$ and of the electronic specific heat coefficient $\gamma(H)$ provides a possible alternative, both datasets being expected to show a distinct field response compared to a single-gap superconductor [52, 61]. For example, $\gamma(H)$ exhibits a clear change in slope when the applied magnetic field suppresses the small gap, a feature recognized as the fingerprint of multigap superconductors. Conversely, $\gamma(H)$ is mostly linear in the single-gap case.

Table I.Normal- and superconducting state properties of C-Re_3B and NC-Re_7B_3, as determined from electrical-resistivity, magnetization, specific-heat, and μSR measurements, as well as electronic band-structure calculations. The London penetration depth λ_L, the effective mass $m^\star$, carrier density n_s, BCS coherence length ξ_0, electronic mean-free path l_e, Fermi velocity v_F, and effective Fermi temperature T_F were estimated following the methods in Ref. 30.

Property	Unit	Re_3B	Re_7B_3
Space group	–	$Cmcm$	$P6_3mc$
Inversion center	–	Yes	No
ρ_0	$\mu\Omega$ cm	68.0	18.5
Residual resistivity ratio	–	1.9	5.8
T_c^ρ	K	5.2	3.5
T_c^χ	K	5.1	3.3
T_c^C	K	4.7	3.1
$T_c^{\mu SR}$	K	4.8	2.9
$\mu_0 H_{c1}$	mT	5.4(1)	7.8(1)
$\mu_0 H_{c2}$	T	3.5(1)	1.05(5)
γ_n	mJ/mol-K^2	9.6(1)	21.5(2)
Θ_D	K	390(3)	440(5)
$N(\epsilon_F)^C$	states/eV-f.u.	4.1(1)	9.1(1)
$N(\epsilon_F)^{DFT}$	states/eV-f.u.	2.35	5.7
$\Delta_0(C)$	meV	0.75(2)	0.47(1)
$\Delta_0(\mu SR)^{clean}$	meV	0.77(2)	0.50(2)
$\Delta_0(\mu SR)^{dirty}$	meV	0.66(2)	0.44(1)
w	–	0.7	0.27
$\Delta_0^f(C)$	meV	0.69(2)	0.32(1)
$\Delta_0^s(C)$	meV	0.79(2)	0.50(1)
$\Delta_0^f(\mu SR)$	meV	0.72(1)	0.35(1)
$\Delta_0^s(\mu SR)$	meV	0.87(2)	0.57(2)
λ_0	nm	263(2)	261(2)
$\lambda_{GL}(0)$	nm	353(4)	259(2)
$\xi(0)$	nm	9.7(1)	17.7(4)
κ	–	36(1)	14.6(5)
λ_L	nm	90(5)	229(2)
l_e	nm	2.2(1)	22(1)
ξ_0	nm	17(1)	6.4(1)
ξ_0/l_e	–	7.7	0.3
$m^\star$	m_e	7.0(2)	10.4(1)
n_s	10^{28} m^{-3}	2.4(3)	0.56(1)
v_F	10^5 ms^{-1}	1.5(1)	0.61(1)
T_F	10^4 K	1.0(1)	0.25(1)

Finally, we discuss about the effects of a lack of inversion symmetry in Re_7B_3. In NCSCs, the antisymmetric spin-orbit coupling (ASOC) allows for the occurrence of an admixture of singlet and triplet pairings, whose mixing degree is generally believed to be related to the strength of the ASOC [1] and, thus, to unconventional SC. Here by comparing NC-Re_7B_3 with C-Re_3B, we found that a noncentrosymmetric structure and its accompanying ASOC have little effect on the superconducting properties of Re_7B_3. First, the upper critical field of NC-Re_7B_3 is three times smaller than that of C-Re_3B, in both cases H_{c2} being well below the Pauli limit. Second, according to the ZF-μSR data (Fig. 3), TRS is preserved in the superconducting states of both samples. The new results presented here further support the idea that the rhenium presence and its amount are the two key factors which determine the appearance of TRS breaking in Re-based superconductors, while the noncentrosymmetric structure plays only a marginal role. Obviously, the Re-content in both Re_3B and Re_7B_3 might be below the threshold value, e.g., 88% in Re-Mo alloys [30]. Therefore, it could be interesting to check, upon increasing the Re-content, whether the TRS breaking effect will appear also in the rhenium-boron superconductors. Third, both Re_7B_3 and Re_3B exhibit nodeless SC with multiple gaps. In case of Re_7B_3, whether the multigap feature is due to the band splitting caused by the ASOC, or to the multiple bands crossing its Fermi level (the latter, in principle, accounting also for the C-Re_3B case), requires further theoretical work. Overall, as can be seen from Fig. 6(b), the ASOC and the band splitting is relatively small in Re_7B_3. Hence, we expect the spin-singlet pairing to be dominant in both the centrosymmetric and noncentrosymmetric rhenium-boron superconductors.

IV. CONCLUSION

To summarize, we studied the superconducting properties of the centrosymmetric Re_3B and the noncentrosymmetric Re_7B_3 superconductors by means of electrical resistivity, magnetization, heat capacity, and μSR techniques, as well as via numerical calculations. The superconducting state of Re_3B and Re_7B_3 is characterized by $T_c = 5.1$ K and 3.3 K, and upper critical fields $\mu_0 H_{c2}(0) = 3.5$ T and 1.05 T, respectively. The temperature-dependent zero-field electronic specific heat and superfluid density reveal a *nodeless* superconductivity, well described by an *isotropic s-wave* model. Both Re_3B and Re_7B_3 exhibit a positive curvature in their temperature-dependent upper critical field $H_{c2}(T)$, an established fingerprint of multigap superconductivity. By combining our extensive experimental results with numerical band-structure calculations, we provide evidence regarding multigap superconductivity in both centro- and noncentrosymmetric rhenium-boron superconductors. Finally, the lack of spontaneous magnetic fields below T_c indicates that, unlike in the ReT or elementary rhenium, the time-reversal symmetry is *preserved* in the superconducting state of both Re_3B and Re_7B_3. Our results suggest that the spin-singlet paring channel is dominant in the rhenium-boron superconductors.

Note. While preparing the current manuscript, we became aware of a related work by S. Sharma et al. [66], in which similar compounds were studied via the μSR technique.

ACKNOWLEDGMENTS

This work was supported by start funding from East-China Normal University (ECNU), the Swiss SNF Grants (No. 200021-169455 and No. 206021-139082) and the Sino-Swiss Science and Technology Cooperation (Grant No. IZLCZ2-170075). H.Q.Y. acknowledges support from the National Key R&D Program of China (No. 2017YFA0303100 and No. 2016YFA0300202), the Key R&D Program of Zhejiang Province, China (No. 2021C01002), the National Natural Science Foundation of China (No. 11974306). We acknowledge the allocation of beam time at the Swiss muon

source, and thank the scientists of Dolly μSR spectrometer for their support.

[1] E. Bauer and M. Sigrist, eds., *Non-Centrosymmetric Superconductors*, Vol. 847 (Springer Verlag, Berlin, 2012).

[2] M. Smidman, M. B. Salamon, H. Q. Yuan, and D. F. Agterberg, Superconductivity and spin–orbit coupling in non-centrosymmetric materials: A review, Rep. Prog. Phys. **80**, 036501 (2017).

[3] S. K. Ghosh, M. Smidman, T. Shang, J. F. Annett, A. D. Hillier, J. Quintanilla, and H. Yuan, Recent progress on superconductors with time-reversal symmetry breaking, J. Phys.: Condens. Matter **33**, 033001 (2021).

[4] H. Kim, K. Wang, Y. Nakajima, R. Hu, S. Ziemak, P. Syers, L. Wang, H. Hodovanets, J. D. Denlinger, P. M. R. Brydon, D. F. Agterberg, M. A. Tanatar, R. Prozorov, and J. Paglione, Beyond triplet: Unconventional superconductivity in a spin-3/2 topological semimetal, Sci. Adv. **4**, eaao4513 (2018).

[5] Z. X. Sun, M. Enayat, A. Maldonado, C. Lithgow, E. Yelland, D. C. Peets, A. Yaresko, A. P. Schnyder, and P. Wahl, Dirac surface states and nature of superconductivity in noncentrosymmetric BiPd, Nat. Commun. **6**, 6633 (2015).

[6] M. N. Ali, Q. D. Gibson, T. Klimczuk, and R. J. Cava, Noncentrosymmetric superconductor with a bulk three-dimensional Dirac cone gapped by strong spin-orbit coupling, Phys. Rev. B **89**, 020505(R) (2014).

[7] M. Sato and S. Fujimoto, Topological phases of noncentrosymmetric superconductors: Edge states, Majorana fermions, and non-Abelian statistics, Phys. Rev. B **79**, 094504 (2009).

[8] Y. Tanaka, Y. Mizuno, T. Yokoyama, K. Yada, and M. Sato, Anomalous Andreev bound state in noncentrosymmetric superconductors, Phys. Rev. Lett. **105**, 097002 (2010).

[9] M. Sato and Y. Ando, Topological superconductors: A review, Rep. Prog. Phys. **80**, 076501 (2017).

[10] X.-L. Qi and S.-C. Zhang, Topological insulators and superconductors, Rev. Mod. Phys. **83**, 1057 (2011).

[11] C. Kallin and J. Berlinsky, Chiral superconductors, Rep. Prog. Phys. **79**, 054502 (2016).

[12] E. M. Carnicom, W. Xie, T. Klimczuk, J. J. Lin, K. Górnicka, Z. Sobczak, N. P. Ong, and R. J. Cava, $TaRh_2B_2$ and $NbRh_2B_2$: Superconductors with a chiral noncentrosymmetric crystal structure, Sci. Adv. **4**, eaar7969 (2018).

[13] E. Bauer, G. Hilscher, H. Michor, C. Paul, E. W. Scheidt, A. Gribanov, Y. Seropegin, H. Noël, M. Sigrist, and P. Rogl, Heavy fermion superconductivity and magnetic order in noncentrosymmetric $CePt_3Si$, Phys. Rev. Lett. **92**, 027003 (2004).

[14] H. Q. Yuan, D. F. Agterberg, N. Hayashi, P. Badica, D. Vandervelde, K. Togano, M. Sigrist, and M. B. Salamon, *s*-wave spin-triplet order in superconductors without inversion symmetry: Li_2Pd_3B and Li_2Pt_3B, Phys. Rev. Lett. **97**, 017006 (2006).

[15] M. Nishiyama, Y. Inada, and G.-q. Zheng, Spin triplet superconducting state due to broken inversion symmetry in Li_2Pt_3B, Phys. Rev. Lett. **98**, 047002 (2007).

[16] I. Bonalde, W. Brämer-Escamilla, and E. Bauer, Evidence for line nodes in the superconducting energy gap of noncentrosymmetric $CePt_3Si$ from magnetic penetration depth measurements, Phys. Rev. Lett. **94**, 207002 (2005).

[17] T. Shang, M. Smidman, A. Wang, L.-J. Chang, C. Baines, M. K. Lee, Z. Y. Nie, G. M. Pang, W. Xie, W. B. Jiang, M. Shi, M. Medarde, T. Shiroka, and H. Q. Yuan, Simultaneous nodal superconductivity and time-reversal symmetry breaking in the noncentrosymmetric superconductor CaPtAs, Phys. Rev. Lett. **124**, 207001 (2020).

[18] S. Kuroiwa, Y. Saura, J. Akimitsu, M. Hiraishi, M. Miyazaki, K. H. Satoh, S. Takeshita, and R. Kadono, Multigap superconductivity in sesquicarbides La_2C_3 and Y_2C_3, Phys. Rev. Lett. **100**, 097002 (2008).

[19] A. D. Hillier, J. Quintanilla, and R. Cywinski, Evidence for time-reversal symmetry breaking in the noncentrosymmetric superconductor $LaNiC_2$, Phys. Rev. Lett. **102**, 117007 (2009).

[20] J. A. T. Barker, D. Singh, A. Thamizhavel, A. D. Hillier, M. R. Lees, G. Balakrishnan, D. M. Paul, and R. P. Singh, Unconventional superconductivity in La_7Ir_3 revealed by muon spin relaxation: Introducing a new family of noncentrosymmetric superconductor that breaks time-reversal symmetry, Phys. Rev. Lett. **115**, 267001 (2015).

[21] D. Singh, M. S. Scheurer, A. D. Hillier, D. T. Adroja, and R. P. Singh, Time-reversal-symmetry breaking and unconventional pairing in the noncentrosymmetric superconductor La_7Rh_3, Phys. Rev. B **102**, 134511 (2020).

[22] D. A. Mayoh, A. D. Hillier, G. Balakrishnan, and M. R. Lees, Evidence for the coexistence of time-reversal symmetry breaking and Bardeen-Cooper-Schrieffer-like superconductivity in La_7Pd_3, Phys. Rev. B **103**, 024507 (2021).

[23] T. Shang, S. K. Ghosh, J. Z. Zhao, L.-J. Chang, C. Baines, M. K. Lee, D. J. Gawryluk, M. Shi, M. Medarde, J. Quintanilla, and T. Shiroka, Time-reversal symmetry breaking in the noncentrosymmetric Zr_3Ir superconductor, Phys. Rev. B **102**, 020503(R) (2020).

[24] R. P. Singh, A. D. Hillier, B. Mazidian, J. Quintanilla, J. F. Annett, D. M. Paul, G. Balakrishnan, and M. R. Lees, Detection of time-reversal symmetry breaking in the noncentrosymmetric superconductor Re_6Zr using muon-spin spectroscopy, Phys. Rev. Lett. **112**, 107002 (2014).

[25] D. Singh, J. A. T. Barker, A. Thamizhavel, D. M. Paul, A. D. Hillier, and R. P. Singh, Time-reversal symmetry breaking in the noncentrosymmetric superconductor Re_6Hf: Further evidence for unconventional behavior in the α-Mn family of materials, Phys. Rev. B **96**, 180501(R) (2017).

[26] T. Shang, G. M. Pang, C. Baines, W. B. Jiang, W. Xie, A. Wang, M. Medarde, E. Pomjakushina, M. Shi, J. Mesot, H. Q. Yuan, and T. Shiroka, Nodeless superconductivity and time-reversal symmetry breaking in the noncentrosymmetric superconductor $Re_{24}Ti_5$, Phys. Rev. B **97**, 020502(R) (2018).

[27] T. Shang, M. Smidman, S. K. Ghosh, C. Baines, L. J. Chang, D. J. Gawryluk, J. A. T. Barker, R. P. Singh, D. M. Paul, G. Balakrishnan, E. Pomjakushina, M. Shi, M. Medarde, A. D. Hillier, H. Q. Yuan, J. Quintanilla, J. Mesot, and T. Shiroka, Time-reversal symmetry breaking in Re-based superconductors, Phys. Rev. Lett. **121**, 257002 (2018).

[28] W. Xie, P. R. Zhang, B. Shen, W. B. Jiang, G. M. Pang, T. Shang, C. Gao, M. Smidman, and H. Q. Yuan, CaPtAs: a new noncentrosymmetric superconductor, Sci. China-Phys. Mech. Astron. **63**, 237412 (2020).

[29] T. Shang, D. J. Gawryluk, J. A. T. Verezhak, E. Pomjakushina, M. Shi, M. Medarde, J. Mesot, and T. Shiroka, Structure and superconductivity in the binary $Re_{1-x}Mo_x$ alloys, Phys. Rev. Materials **3**, 024801 (2019).

[30] T. Shang, C. Baines, L.-J. Chang, D. J. Gawryluk, E. Pomjakushina, M. Shi, M. Medarde, and T. Shiroka, $Re_{1-x}Mo_x$ as an ideal test case of time-reversal symmetry breaking in unconventional superconductors, npj Quantum Mater. **5**, 76 (2020).

[31] A. A. Aczel, T. J. Williams, T. Goko, J. P. Carlo, W. Yu, Y. J. Uemura, T. Klimczuk, J. D. Thompson, R. J. Cava, and G. M. Luke, Muon spin rotation/relaxation measurements of the noncentrosymmetric superconductor $Mg_{10}Ir_{19}B_{16}$, Phys. Rev. B **82**, 024520 (2010).

[32] D. Singh, J. A. T. Barker, A. Thamizhavel, A. D. Hillier, D. M. Paul, and R. P. Singh, Superconducting properties and μSR study of the noncentrosymmetric superconductor $Nb_{0.5}Os_{0.5}$, J. Phys.: Condens. Mat. **30**, 075601 (2018).

[33] P. K. Biswas, A. D. Hillier, M. R. Lees, and D. M. Paul, Comparative study of the centrosymmetric and noncentrosymmetric superconducting phases of Re_3W using muon spin spectroscopy and heat capacity measurements, Phys. Rev. B **85**, 134505 (2012).

[34] J. A. T. Barker, B. D. Breen, R. Hanson, A. D. Hillier, M. R. Lees, G. Balakrishnan, D. M. Paul, and R. P. Singh, Superconducting and normal-state properties of the noncentrosymmetric superconductor Re_3Ta, Phys. Rev. B **98**, 104506 (2018), and references therein.

[35] A. Kawano, Y. Mizuta, H. Takagiwa, T. Muranaka, and J. Akimitsu, The superconductivity in Re-B system, J. Phys. Soc. Jpn. **72**, 1724 (2003).

[36] H. Takagiwa, A. Kawano, Y. Mizuta, T. Yamamoto, M. Yamada, K. Ohishi, T. Muranaka, J. Akimitsu, W. Higemoto, and R. Kadono, Magnetic penetration depth of a new boride superconductor Re_3B, Physica B **326**, 355 (2003).

[37] C. S. Lue, Y. F. Tao, and T. H. Su, Comparative NMR investigation of the Re-based borides, Phys. Rev. B **78**, 033107 (2008).

[38] K. Matano, S. Maeda, H. Sawaoka, Y. Muro, T. Takabatake, B. Joshi, S. Ramakrishnan, K. Kawashima, J. Akimitsu, and G.-q. Zheng, NMR and NQR studies on non-centrosymmetric superconductors Re_7B_3, LaBiPt, and BiPd, J. Phys. Soc. Jpn. **82**, 084711 (2013).

[39] For details on the measurements of crystal structure, electrical resistivity, magnetization, and heat capacity, as well as for the data analysis, see the Supplementary Material at http://link.aps.org/supplemental/XXX/PhysRevB.XXX.

[40] A. Suter and B. M. Wojek, Musrfit: A free platform-independent framework for μSR data analysis, Phys. Procedia **30**, 69 (2012).

[41] J. P. Perdew, K. Burke, and M. Ernzerhof, Generalized gradient approximation made simple, Phys. Rev. Lett. **77**, 3865 (1996).

[42] P. Giannozzi, S. Baroni, N. Bonini, M. Calandra, R. Car, C. Cavazzoni, D. Ceresoli, G. L. Chiarotti, M. Cococcioni, I. Dabo, A. D. Corso, S. d. Gironcoli, S. Fabris, G. Fratesi, R. Gebauer, U. Gerstmann, C. Gougoussis, A. Kokalj, M. Lazzeri, L. Martin-Samos, N. Marzari, F. Mauri, R. Mazzarello, S. Paolini, A. Pasquarello, L. Paulatto, C. Sbraccia, S. Scandolo, G. Sclauzero, A. P. Seitsonen, A. Smogunov, P. Umari, and R. M. Wentzcovitch, QUANTUM ESPRESSO: a modular and open-source software project for quantum simulations of materials, J. Phys. Condens. Matter **21**, 395502 (2009).

[43] P. Giannozzi, O. Andreussi, T. Brumme, O. Bunau, M. B. Nardelli, M. Calandra, R. Car, C. Cavazzoni, D. Ceresoli, M. Cococcioni, N. Colonna, I. Carnimeo, A. D. Corso, S. d. Gironcoli, P. Delugas, R. A. D. Jr, A. Ferretti, A. Floris, G. Fratesi, G. Fugallo, R. Gebauer, U. Gerstmann, F. Giustino, T. Gorni, J. Jia, M. Kawamura, H.-Y. Ko, A. Kokalj, E. Küçükbenli, M. Lazzeri, M. Marsili, N. Marzari, F. Mauri, N. L. Nguyen, H.-V. Nguyen, A. Otero-de-la Roza, L. Paulatto, S. Poncé, D. Rocca, R. Sabatini, B. Santra, M. Schlipf, A. P. Seitsonen, A. Smogunov, I. Timrov, T. Thonhauser, P. Umari, N. Vast, X. Wu, and S. Baroni, Advanced capabilities for materials modelling with Quantum ESPRESSO, J. Phys. Condens. Matter **29**, 465901 (2017).

[44] P. E. Blöchl, Projector augmented-wave method, Phys. Rev. B **50**, 17953 (1994).

[45] A. D. Corso, Pseudopotentials periodic table: From H to Pu, Comput. Mater. Sci. **95**, 337 (2014).

[46] X. Zhu, H. Yang, L. Fang, G. Mu, and H.-H. Wen, Upper critical field, Hall effect and magnetoresistance in the iron-based layered superconductor $LaFeAsO_{0.9}F_{0.1-\delta}$, Supercond. Sci. Technol. **21**, 105001 (2008).

[47] N. R. Werthamer, E. Helfand, and P. C. Hohenberg, Temperature and purity dependence of the superconducting critical field, H_{c2}. III. Electron spin and spin-orbit effects, Phys. Rev. **147**, 295 (1966).

[48] A. Gurevich, Iron-based superconductors at high magnetic fields, Rep. Prog. Phys **74**, 124501 (2011), and references therein.

[49] Y. Nakajima, H. Hidaka, T. Nakagawa, T. Tamegai, T. Nishizaki, T. Sasaki, and N. Kobayashi, Two-band superconductivity featuring different anisotropies in the ternary iron silicide $Lu_2Fe_3Si_5$, Phys. Rev. B **85**, 174524 (2012).

[50] K.-H. Müller, G. Fuchs, A. Handstein, K. Nenkov, V. N. Narozhnyi, and D. Eckert, The upper critical field in superconducting MgB_2, J. Alloys Compd. **322**, L10 (2001).

[51] A. Gurevich, S. Patnaik, V. Braccini, K. H. Kim, C. Mielke, X. Song, L. D. Cooley, S. D. Bu, D. M. Kim, J. H. Choi, L. J. Belenky, J. Giencke, M. K. Lee, W. Tian, X. Q. Pan, A. Siri, E. E. Hellstrom, C. B. Eom, and D. C. Larbalestier, Very high upper critical fields in MgB_2 produced by selective tuning of impurity scattering, Supercond. Sci. Technol. **17**, 278 (2004).

[52] T. Shang, W. Xie, D. J. Gawryluk, R. Khasanov, J. Z. Zhao, M. Medarde, M. Shi, H. Q. Yuan, E. Pomjakushina, and T. Shiroka, Multigap superconductivity in the Mo_5PB_2 boron–phosphorus compound, New J. Phys. **22**, 093016 (2020).

[53] A. Maisuradze, R. Khasanov, A. Shengelaya, and H. Keller, Comparison of different methods for analyzing μSR line shapes in the vortex state of type-II superconductors, J. Phys.: Condens. Mat. **21**, 075701 (2009), and references therein.

[54] E. H. Brandt, Properties of the ideal Ginzburg-Landau vortex lattice, Phys. Rev. B **68**, 054506 (2003).

[55] W. Barford and J. M. F. Gunn, The theory of the measurement of the London penetration depth in uniaxial type-II superconductors by muon spin rotation, Physica C **156**, 515 (1988).

[56] R. Kubo and T. Toyabe, A stochastic model for low-field resonance and relaxation, in *Magnetic Resonance and Relaxation. Proceedings of the XIVth Colloque Ampère*, edited by R. Blinc (North-Holland, Amsterdam, 1967) pp. 810–823.

[57] A. Yaouanc and P. D. de Réotier, *Muon Spin Rotation, Relaxation, and Resonance: Applications to Condensed Matter* (Oxford University Press, Oxford, 2011).

[58] A. Carrington and F. Manzano, Magnetic penetration depth of MgB_2, Physica C **385**, 205 (2003).

[59] M. Tinkham, *Introduction to Superconductivity*, 2nd ed. (Dover Publications, Mineola, NY, 1996).

[60] Y. J. Uemura, L. P. Le, G. M. Luke, B. J. Sternlieb, W. D. Wu, J. H. Brewer, T. M. Riseman, C. L. Seaman, M. B. Maple, M. Ishikawa, D. G. Hinks, J. D. Jorgensen, G. Saito, and H. Yamochi, Basic similarities among cuprate, bismuthate, organic, Chevrel-phase, and heavy-fermion superconductors shown by penetration-depth measurements, Phys. Rev. Lett. **66**, 2665 (1991).

[61] T. Shang, A. Amon, D. Kasinathan, W. Xie, M. Bobnar, Y. Chen, A. Wang, M. Shi, M. Medarde, H. Q. Yuan, and T. Shiroka, Enhanced T_c and multiband superconductivity in the fully-gapped $ReBe_{22}$ superconductor, New J. Phys. **21**, 073034 (2019).

[62] Y. J. Uemura, Twin spin/charge roton mode and superfluid density: Primary determining factors of T_c in high-T_c superconductors observed by neutron, ARPES, and μSR, Physica B **374**, 1 (2006).

[63] Y. Xu, S. Jöhr, L. Das, J. Kitagawa, M. Medarde, T. Shiroka, J. Chang, and T. Shang, Crossover from multiple- to single-gap superconductivity in $Nb_5Ir_{3-x}Pt_xO$ alloys, Phys. Rev. B **101**, 134513 (2020).

[64] T. Shang, J. Philippe, J. A. T. Verezhak, Z. Guguchia, J. Z. Zhao, L.-J. Chang, M. K. Lee, D. J. Gawryluk, E. Pomjakushina, M. Shi, M. Medarde, H.-R. Ott, and T. Shiroka, Nodeless superconductivity and preserved time-reversal symmetry in the noncentrosymmetric Mo_3P superconductor, Phys. Rev. B **99**, 184513 (2019).

[65] V. G. Kogan, C. Martin, and R. Prozorov, Superfluid density and specific heat within a self-consistent scheme for a two-

band superconductor, Phys. Rev. B **80**, 014507 (2009).
[66] S. Sharma, Arushi, K. Motla, J. Beare, M. Nugent, M. Pula, T. J. Munsie, A. D. Hillier, R. P. Singh, and G. M. Luke, Fully gapped superconductivity in centrosymmetric and noncentrosymmetric Re-B compounds probed with μSR, Phys. Rev. B **103**, 104507 (2021).